2020 IEEE International Conference on Robotics and Automation (ICRA)
31 May - 31 August, 2020. Paris, France

Towards distortion based underwater domed viewport camera calibration

Eduardo Iscar[1], Matthew Johnson-Roberson[1]

Abstract— **Photogrammetry techniques used for 3D reconstructions and motion estimation from images are based on projective geometry that models the image formation process. However, in the underwater setting, refraction of light rays at the housing interface introduce non-linear effects in the image formation. These effects produce systematic errors if not accounted for, and severely degrade the quality of the acquired images. In this paper, we present a novel approach to the calibration of cameras inside spherical domes with large offsets between dome and camera centers. Such large offsets not only amplify the effect of refraction, but also introduce blur in the image that corrupts feature extractors used to establish image-world correspondences in existing refractive calibration methods. We propose using the point spread function (PSF) as a complete description of the optical system and introduce a procedure to recover the camera pose inside the dome based on the measurement of the distortions. Results on a collected dataset show the method is capable of recovering the camera pose with high accuracy.**

I. Introduction

In recent decades, computer vision techniques, such as photogrammetric 3D reconstructions or visual navigation, have seen a great increase in applications to the underwater domain. Examples include coral reef surveys [1], 3D reconstruction [2], benthic population assessment [3], or ship hull inspection [4]. Algorithms used for aerial or terrestrial environments are frequently used for underwater visual odometry (VO) [5] or photogrammetric 3D reconstructions [6]. However, to deploy cameras in the aqueous environment, underwater optical systems require an additional housing that protects the lens and camera from water damage as well as pressure. Light rays travelling through this additional housing interface get refracted when changing mediums. The change in direction is proportional to the incidence angle and the quotient of the materials refractive indices. Due to refraction, camera rays no longer intersect the optical axis at the center of projection [7]. Underwater images are further affected by scattering and absorption, a wavelength dependent phenomenon that modifies the perceived color in the images. As a consequence, the widely used pinhole camera model [8] is no longer valid [9].

Most underwater housings fall into two main categories: flat viewports and domed viewports. Flat viewports are simpler to manufacture and generally smaller. However, they reduce the camera field of view (FOV) by approximately 25% [10]. Inversely, domed viewports are more difficult to manufacture, but do not introduce refraction effects in the image as long as the center of the dome and the camera optical center are located at the same position. Although this is very difficult to achieve in practice, it has been shown in [11] that the error is negligible when the misalignment is small. However, there are situations where it is not possible to align the optical center of the camera with the center of the dome, such as when multiple cameras share a single domed viewport. Figure 1 shows such a stereo camera pair housed in a borosilicate glass sphere. This sphere is used as the main pressure housing for the DROP-Sphere, a novel, low-cost deep sea autonomous underwater vehicle (AUV) being developed by the authors [12]. Using a glass sphere as the main pressure vessel drastically reduces the AUV's cost to a total less than $\$35,000$, enabling access to the deep ocean for a much wider community of researchers and scientists. One of the main characteristics of the DROP-Sphere is that it dispenses with the Doppler velocity log (DVL) and relies on the camera feed for its navigation while surveying the ocean benthos. As a consequence, it is required to address the errors arising from large offsets in domed underwater cameras to enable accurate vehicle navigation and precise 3D reconstructions of the ocean seafloor. This paper analyzes the applicability of methods developed for domed housings with small offsets and introduces the usage of the point spread function (PSF) as a means to compute the camera position inside the dome. To do so, we collect a dataset of PSFs for multiple camera-dome positions and show how the camera pose can be recovered by analysing the optical distortions.

Fig. 1: Stereo camera used for vehicle navigation. The position of the cameras is far from the center of the hemisphere, introducing significant distortion in the images.

More specifically, the contributions of this paper are two fold. First, we analyze raytracing, a technique frequently used in the literature for underwater refractive models, and show how and why it fails in the case of domed viewports

[1]Eduardo Iscar and Matthew Johnson-Roberson are with the Department of Naval Architecture and Marine Engineering, University of Michigan, Ann Arbor, MI 48109 USA {eiscar,mattjr}@umich.edu

with large camera-dome offsets. Second, we propose the use of the PSF to characterize the complete optical system consisting of camera, lens, and dome, and use it to obtain the camera pose within the dome.

II. Related Work

Modelling underwater image formation effects has been an important topic of research in recent years. Extensive work has been done with regard to the effect of flat viewport lenses on underwater cameras. A comprehensive overview of the literature on refractive underwater imaging and camera models is presented by Sedlazeck et. al. [9]. A popular approach has been to use an unmodified pinhole camera model [8] together with a conventional calibration based on checkerboard patterns [13] performed underwater. Errors due to refraction, attenuation, and scattering are absorbed by the estimated camera intrinsic and distortion parameters. It is important to realize that pinhole calibrations performed underwater at a specific distance are able to achieve very low reprojection errors of the calibration features due to the available degrees of freedom in the distortion coefficients, camera intrinsics, and pose. For such calibrations, however, errors appear both in camera translation and rotation, with large displacements from the true values.. Projection of points, and camera raytracing will be affected by such systematic errors that are dependent on scene depth. In previous work [14], we analyzed the implications of such systematic errors on the accuracy of underwater 3D reconstructions. However, examples of the successful application of this approach are numerous in the literature [15] [16]. Other authors propose to slightly modify the pinhole camera model for underwater use. Lavest et al. [10] analyzed the effect of flat viewports on the camera calibration and established that the effective focal length underwater is 1.33 times the focal length in air. Their derivation, however, only holds for viewports with a constant surface normal and does not generalize to domed housings.

Flat viewports also require the estimation of extra parameters to completely calibrate the imaging system. In addition to the camera extrinsics $[R|t]$, distortion parameters d and intrinsics K, the distance between the camera and flat viewport, and the viewport normal, need to be estimated. Sedlazeck and Koch [17] present a calibration method for flat viewport stereo cameras that does not require any special calibration target to be imaged. Additional parameters, such as interface thickness or refractive indices, can also be included in the calibration process. Sedlazeck and Koch [18] developed such a method that also includes the estimation of the parameters of a radiometric model of light propagation. Much less work has been done to model, characterize, and correct refraction in domed viewports. One of the main reasons is that domed viewports introduce smaller distortions when properly aligned. Kunz and Singh [11] used raytracing to simulate refraction through a spherical interface and evaluate the induced error in 3D point triangulation. However, the authors focused on small displacements between the dome center and the optical center and did not consider situations where the offset is large compared to the hemisphere radius. Additionally, their experiments are limited to simulation. Bosch et al. [19] implemented a similar calibration method for an omnidirectional camera system in a cylindrical and spherical housing based on non-linear optimization of camera intrinsics, extrinsics, and housing parameters using raytracing. Their work, however, shows limited quantitative evaluation of the calibration results and requires high quality images for feature extraction. Related work by Menna et al. [20] presented methods for characterization of a commercial underwater camera domed housing and analyzed its properties.

While these methods approach refractive image formation from a physics-based perspective, extensive work has been done in the image processing community to recover images that are degraded by a range of different effects, such as motion blur, chromatic aberrations, comma, or defocus. This process generally assumes that the observed image can be expressed as the convolution of the underlying "sharp" image with an unknown kernel, called the PSF. If the PSF for a system is known, the original, undegraded image can be recovered through deconvolution. The characterization of the optical distortions through the PSF forms the foundation of the method introduced in this paper for domed housing camera calibration and is described in detail in Section IV.

III. Limitations of ray tracing methods

As mentioned in Section II, most previous work focuses on the modelling of refraction by tracing individual light rays imaged by the camera and explicitly computing the refraction points at each of the interfaces. Most developed methods rely heavily on a constant interface, normal in the case of flat viewports, while, to the best of our knowledge, only domed housing simulation results have been presented. In this Section, we analyze the issues arising when raytracing methods are applied to the calibration of cameras with large offsets in spherical dome housings (Section III-A) and describe the main sources of image degradation (Section III-B). The raytracing process is visualized in Figure 2. The figure shows a ray originating from the camera at a given pixel that intersects the inner glass surface at point **A**, with angle θ. While going through the interface, the ray is refracted according to Snell's Law and then travels through the glass until it intersects the outer surface at point **B**. At this point, it is refracted again and the ray direction in water can be obtained. This generates a set of *image pixel - underwater ray* correspondences that fully describe a general camera model and allow to obtain the camera ray in water for any given pixel coordinate. The inverse of this problem, to obtain the pixel that corresponds to a given 3D point, is called reprojection and has to be solved as an optimization problem due to the nonlinearities introduced by refraction. The reader is referred to [11], [21] for more information on general camera models and ray equation derivations.

A. Raytracing based calibration

In the context of most computer vision applications, the pinhole camera model [8] is used together with a calibration

technique based on the imaging of geometric patterns such as checkerboards [13], circle grids or AprilTags [22] to establish correspondences between pixel coordinates and 3D world coordinates. The raytracing underwater image formation model requires a total of 24 parameters in the case of spherical dome housings: 4 camera intrinsic (K) parameters (focal length for each image axis and image center), 5 lens distortion parameters (3 radial and 2 tangential coefficients), 6 pose parameters each for the camera and dome poses respectively, as well as the three refraction coefficients of air, glass, and water. The camera intrinsic and distortion coefficients can be obtained by performing a pinhole camera calibration in air [13]. Furthermore, due to the rotational symmetry of the dome, the camera pose with respect to the dome reduces to the estimation of its translation vector. Finally, refraction coefficients for the glass interface can be obtained from manufacturer data with high accuracy using the Sellmeier Equation [23]. While the refractive index of air depends on temperature and pressure, changes are under 0.008% [24]. The index of refraction of sea water is the most variable of the three with up to 3%, but given pressure, temperature, and salinity, its value can be computed with an accuracy of at least 10^{-4} [25]. With these simplifications, the calibration of a domed underwater camera system only requires the estimation of the relative camera-dome translation $\mathbf{T}_c^{dome}$ and the camera extrinsics ($\mathbf{R}_w^c$ and $\mathbf{T}_w^c$) for each image taken.

Due to the nonlinear effects introduced into the image formation process by refraction, no explicit expression for the model parameters can be derived. Nonlinear optimization methods can be used to search for the correct parameter values through the minimization of a cost function.
Following the procedure outlined in [11], the calibration process is set up as two nested optimization problems. The outer loop optimizes the relative position between the camera and dome, while the inner loop searches for the optimal camera extrinsics $\mathbf{R}_w^c$ and $\mathbf{T}_w^c$.

$$\mathbf{R}_w^c, \mathbf{T}_w^c, \mathbf{T}_c^{dome} = \arg\min \frac{1}{2} \sum_i^n \rho_i \left\| d_i \right\|^2 \tag{1}$$

$$d_i \left(\mathbf{R}_w^c, \mathbf{T}_w^c, \mathbf{T}_c^{dome} \right) = \frac{\left\| BX \times u \right\|}{\left\| u \right\|} \tag{2}$$

where d_i is the distance between the in-water ray defined by the intersection point with the outer surface B, and its direction u going through pixel i and the corresponding 3D point X. We chose to define the cost function as the L2 distance between the ray and 3D point instead of the reprojection error because the reprojection of world points into the image is itself a minimization problem. Instead, the distance can be computed very efficiently.

The initial values for the camera poses are computed through the Efficient Perspective-n-Point (EPNP) algorithm [26], while initial values for the camera to dome's relative position can be either measured on the physical system or CAD model.

Figure 3 shows the result of applying the proposed raytracing-based algorithm to noiseless pixel-3D point correspondences in simulation.The optimizer successfully converged on all noiseless trials and the resulting reprojection error was orders of magnitude smaller than that obtained if a pinhole model was assumed and a calibration performed using in-water checkerboard images. This figure not only highlights how a refractive calibration outperforms a simple pinhole camera model if data can be measured with small enough noise but also shows how pinhole calibrations can achieve misleadingly small reprojection errors when calibrated at a single distance. After performing experiments with noiseless data, the procedure was repeated introducing increasing levels of noise on the corners extracted from the image. The results are shown in Figure 4, showing the histogram of camera pose estimation errors as noise is increased. This figure shows how camera pose estimation performance quickly degrades, even in the presence of pixel noise as low as 4px

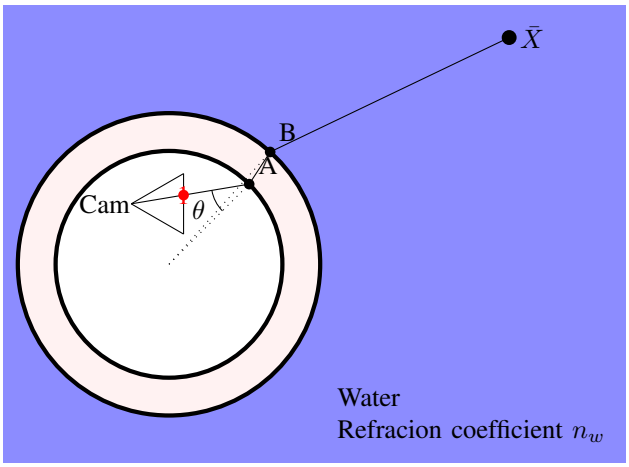

Fig. 2: This figure shows the effect of refraction on underwater image formation. Refraction effects have been exaggerated for illustration purposes.

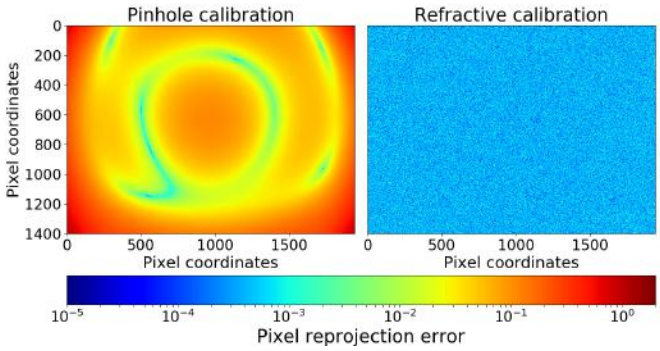

Fig. 3: Result of camera calibration simulations without noise. Both images show the reprojection error of points on a plane at 3m in front of the camera. The left image represents the reprojection using a conventional pinhole camera model calibrated with underwater images; the right image incorporates refraction with the proposed improved model.

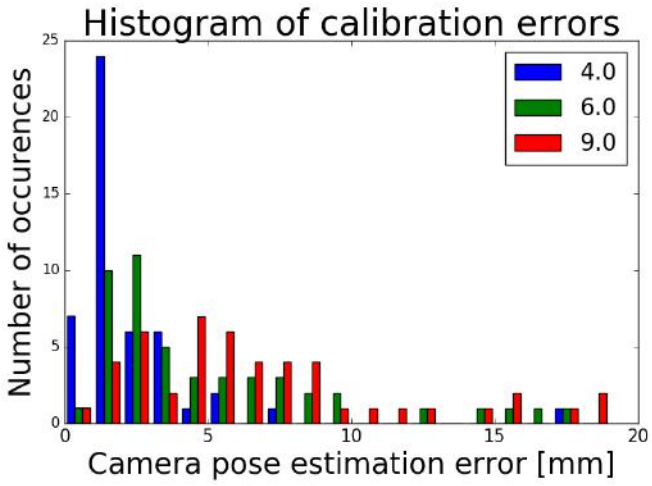

Fig. 4: As pixel noise increases, the calibration optimization converges to local minima at significant distances from the true camera position and ray tracing will fail. Histogram legend in pixels.

B. Sources of error

In addition to refraction-based geometric distortion, images taken inside glass domed viewports are degraded by additional effects exemplified in Figure 5. This figure shows an image of different calibration boards acquired by one of the cameras inside the spherical housing shown in Figure 1 and highlights the following effects: 1) Space varying defocus: The spherical glass interface acts as a lens and generates a space-varying defocus across the image plane. This effect can be seen when comparing the two zoomed areas in the bottom of Figure 5. 2) Chromatic aberration: The different light wavelengths are refracted in different amounts by the interface, generating a change in color. 3) Illumination falloff: Part of the light gets reflected on the glass dome surface in addition to lens vignetting, generating the illumination decay pattern observed.

The large influence of these effects on image formation when large offsets from the dome center are present is the main differentiating factor between the problems addressed by Kunz et al. [11] and Bosch et al. [19], both of which require accurate corner feature extraction. The combination of these effects adds excessive noise to the position of corners extracted from the calibration targets. Multiple attempts were performed to apply the raytracing-based calibration procedure to real datasets with different calibration patterns without success.

IV. Distortion based calibration

A. Image formation

The degradation effects introduced in Section III-B can be encoded as a convolution kernel K. The observed image O is then the result of convolving the kernel with the original image I in the presence of additive gaussian noise N.

$$O = I \circledast K + N \tag{3}$$

The kernel K is known as the PSF. Intuitively, in an ideal optical system a point of light would appear as a single point

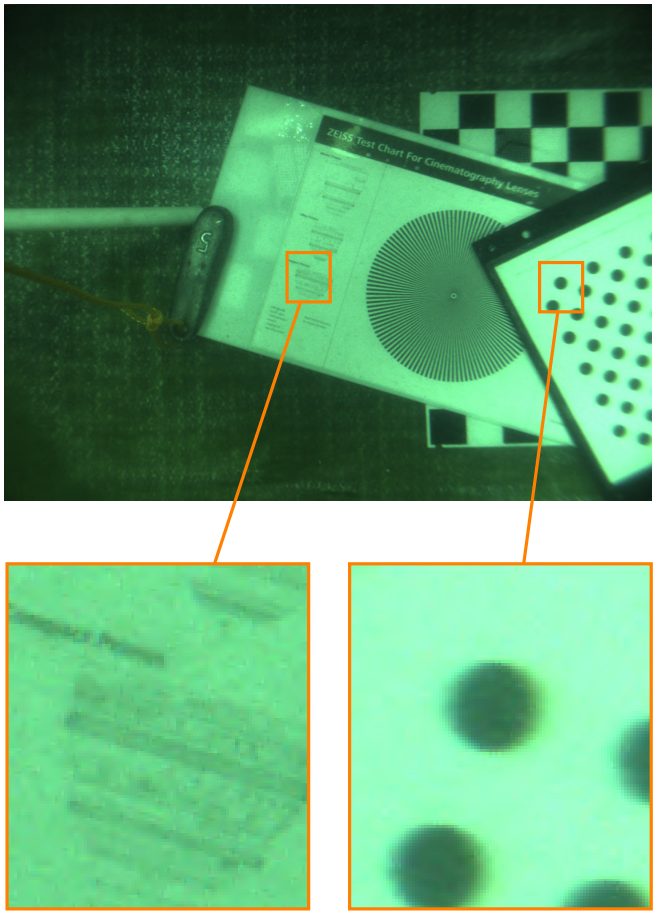

Fig. 5: Example of image obtained inside the dome with large offset from the center. Note the difference in focus across the image plane as well as the chromatic aberration along the circle edges.

in the image, with a one to one correspondence between image plane and object plane. However, in a real imaging system the point image is degraded or spread by the kernel K. Deconvolution can be applied to the observed image O to recover the latent image I. Methods can be divided into blind and non-blind methods. While blind methods estimate both the PSF and latent image simultaneously, non-blind methods provide better results when provided with a prior of the PSF. The PSF is a unique property of an optical system and fully describes it; that is, no two distinct optical systems share the same PSF [27]. As a consequence, if the PSF of a system can be measured, it should be possible to recover the parameters of the system that generated it. It is, however, a very high dimensional function that depends on optical properties, such as lens geometry and materials, aperture, and imaging distance. While in some cases, such as with motion blur, a static PSF can be used for the whole image, the general PSF will also vary along the image plane.

Shih et al. [28] showed that the PSF can be used to refine lens prescription parameters through optimization. Their work focuses, however, on small deviations from the nominal parameters due to manufacturing inaccuracies. Our

work considers the dome-lens-camera system as an optical assembly with large parameter variations.

B. Distortion based calibration

Knowledge about the PSF and its variations with respect to the optical system variables can be used to recover the specific set of parameters that generates the image distortions observed. If we consider the relative position between dome and camera as independent variables of the PSF, obtaining the complete lens prescription is equivalent to calibrating the optical system. Such a priori knowledge about the PSF can be obtained in the form of measurement datasets or high fidelity optical simulations. In this work we focus on the case where a dataset of the PSF for different camera-dome positions is available. Details about dataset collection and experimental setup are given in Section V. If such a dataset of PSFs is available for a discrete set of camera-sphere relative positions, it is now possible to formulate the calibration problem as one where, given a measurement of the PSF, we aim to recover the x, y, and z ($\mathbf{T}_c^{dome}$) position of the camera that generated such an array of distortions. Given a set of measured PSFs, G_{ij}, each centered at pixel i, j, for one system configuration, and a dataset $U_{i,j}(x, y, z)$ of the PSFs for different camera to sphere position x, y and z at the same i, j positions, we define the cost function as

$$f(x, y, z) = \sum_{R,G,B} \sum_{i,j} \|G_{i,j} - P_{i,j}(x, y, z)\| \qquad (4)$$

where $P_{i,j}(x, y, z)$ is the estimated response based on the available dataset. Because PSFs can only be measured at a discrete set of coordinates in the image plane, we use linear interpolation to obtain the PSF at the desired pixel coordinates. In the same way, PSFs can be interpolated between different camera poses [29] to obtain $P_{i,j}$ from $U_{i,j}$.

The camera position inside the dome can then be computed as

$$x, y, z = \arg\min f(x, y, z) \qquad (5)$$

This equation can be solved by means of non-linear least squares algorithms such as Levenberg-Marquardt.

V. Experimental PSF characterization

In order to characterize the changes of the PSF with respect to camera pose inside the spherical dome, we assembled the experimental setup shown in Figure 6. The camera was mounted on a three-axis linear motion stage. The X axis was an electronically controlled, 150mm travel range stage, while both the Y and Z axes were manual, 50mm travel stages. The camera was mounted with the optical axis aligned with the system X axis. On top of the camera was a mounted precision indicator dial, also aligned with the X axis. A custom acrylic tank was assembled to hold one of the BK-7 glass hemispheres used as the pressure housing by the DROP-Sphere in front of the camera. The hemisphere had an external nominal radius of 187mm and a thickness of 14mm. Finally, in the tank, on the opposite side of the spherical dome at a distance of 370mm, a LED light source was mounted on an actuated YZ motion platform controlled by stepper motors. A 0.2mm pinhole cut out of 0.1mm thick stainless steel was placed in front of the LED module to generate a small-point light source. The LED light was configured to emit red, green, and blue light. Using a movable single light point as opposed to a grid of points ensured repeatable measurements and allowed exposure to be adjusted individually for each position to adequately use the cameras sensor dynamic range.

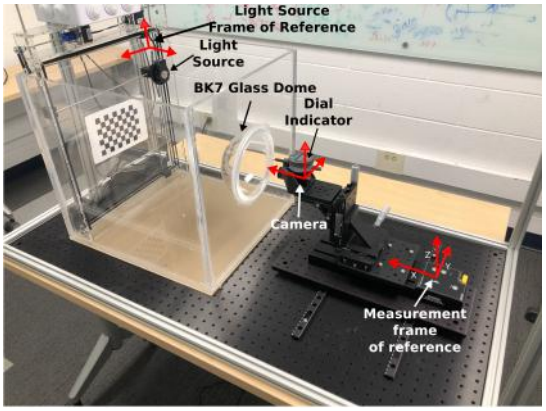

Fig. 6: Experimental setup used to record the PSF of the complete camera-lens-dome optical system for different camera position within the dome. The light source motion system can be seem at the back of the tank.

A. Experimental procedure

For each camera pose, the light source was moved to 62 different YZ positions evenly spaced along the back of the tank. Not all positions fell within the field of view of every camera pose but the experiment was designed so all camera poses had a similar number of measurements taken. For each of the positions, the PSF was measured for red, green, and blue light. Additionally, the focus of the lens was adjusted for each pose. While this change in backfocal distance affects the shape and size of the PSF and makes the solving of Equation 5 significantly harder due to the unmodelled focus variable, the collected dataset was also designed with future work in mind that will benefit from this property.

B. Collected Dataset

A Flir BFS-U3-63S4C camera, with a pixel size of 2.4um and a resolution of 2048x3072, was used with a Edmund Optics UC-8mm lens. The IMX178 color sensor used a color filter array (CFA) in a RGGB Bayer pattern that requires demosaicing of the measured PSF response. Schuler et al. [30] showed that the improvement, when explicitly considering demosaicing in the deconvolution process, only improved the resulting image peak signal-to-noise ratio (PSNR) by an average of 0.4dB. Based on these results, we exclusively demosaiced the raw image to obtain the PSF of each channel. The PSFs of a total of 200 camera poses were characterized during the experiments, with samples taken at 3mm intervals. While the collected dataset is specific to the camera, lens, and dome used, similar datasets can be collected for different

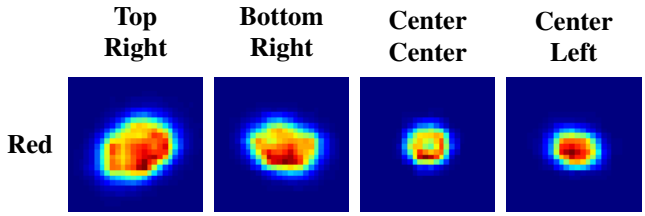

Fig. 7: Examples of the measured point spread functions for four different positions in the image plane for the red light. All PSFs are normalized with respect to their maximum response.

configurations following the outlined procedure. Figure 7 shows the normalized PSFs for the three color channels for four different positions in the image plane and highlights the variability of the PSF as a function of wavelength. Additionally, PSF shape was greatly affected by the position in the image plane and varies between circular blur kernels at the centered to teardrop shaped kernels towards the edges of the image. The size of the PSF greatly increased at the corners, where blur and distortions are maximized.

VI. Results

A. Calibration

The proposed distortion based calibration method (Equation 5) was applied to different poses within the dataset described in Section V. The minimization problem was formulated as a non-linear least squares problem and solved using the Levenberg-Marquardt algorithm. Figure 8 shows the error between the measured and estimated PSF at multiple different positions in the image plane. The optimizer converged to a position with an error of 0.184, 0.004, and 0.023mm on each axis. The error along the X axis is between one and two orders of magnitude larger than the Y and Z axes. Analysing the dataset showed that variation along the X axis mostly affected the size of the PSFs with smaller impact on its shape. Blur caused by a change in focus has a similar influence, being modeled as a solid disk kernel of a varying radius depending on how out of focus the image is. This similarity, together with the previously mentioned fact that the camera focus was readjusted at each pose, is likely the reason for the discrepancy in error magnitude between the axes. Finally, the X axis was sampled very sparsely with only two different values in the dataset, which could further influence the result.

B. Deconvolution

In addition to camera to dome pose calibration, the obtained point spread functions can be used to deconvolve the measured image and recover the underlying image. Figure 9 shows an example of a region of an image before and after deconvolution with the obtained PSF. We used the Van Cittert algorithm as implemented in *DeconvolutionLab2* [31]. In order to evaluate image sharpness, we use the variation of Laplacian, $\sigma^2_{\nabla^2}$ [32], a measure that increases for sharper images. Comparing the original and deconvolved image, values of $\sigma^2_{\nabla^2}$ increased from 19 to 62.

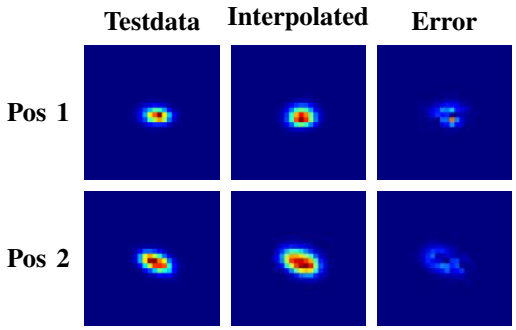

Fig. 8: Resulting PSFs of calibration routine. Each row shows the measured PSF, as well as the result of the optimization at a different position in the image plane. The error plot shows the difference between the test data and optimization and represents a term in Equation 4.

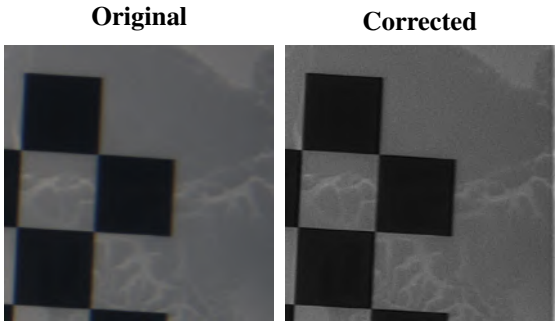

Fig. 9: Deconvolution using the interpolated point spread functions. The variance of the Laplacian, a measure of sharpness, increased from 19.2 to 62.9

VII. Conclusion and Future Work

In this paper, we introduced the use of the PSF as an alternative characterization of an underwater optical system and showed that it can be used to recover the camera position within the dome.

The presented procedure is very time intensive and requires the PSF measurements used for calibration to be performed under the same conditions (such as aperture or working distance) as the dataset was when it was collected. This severely limits the application of the technique on field deployed robotic platforms. Future work will focus on the development of a deep learning-based model trained with extensive datasets of high resolution optical simulations of PSFs. The network will enable fast and efficient regression of the optical system parameters. The simulation software enables the user to adapt the range of optical parameters to the intervals of interest depending on operational constraints. Finally, we are sharing the collected dataset under `https://umich.box.com/v/psfdataset-uwdomedcameras`.

Acknowledgments

The authors would like to acknowledge the insightful comments by the paper's reviewers. The work presented has been partially supported by NASA award NNX16AL08G.

REFERENCES

[1] S. B. Williams, O. Pizarro, J. M. Webster, R. J. Beaman, I. Mahon, M. Johnson-Roberson, and T. C. Bridge, "Autonomous underwater vehicle–assisted surveying of drowned reefs on the shelf edge of the great barrier reef, australia," *Journal of Field Robotics*, vol. 27, no. 5, pp. 675–697, 2010.

[2] M. Johnson-Roberson, O. Pizarro, S. B. Williams, and I. Mahon, "Generation and visualization of large-scale three-dimensional reconstructions from underwater robotic surveys," *Journal of Field Robotics*, vol. 27, no. 1, pp. 21–51, 2010.

[3] M. E. Clarke, N. Tolimieri, and H. Singh, "Using the seabed auv to assess populations of groundfish in untrawlable areas," in *The future of fisheries science in North America*, Springer, 2009, pp. 357–372.

[4] P. Ozog, N. C. Bianco, A. Kim, and R. M. Eustice, "Longterm mapping techniques for ship hull inspection and surveillance using an autonomous underwater vehicle," *Journal of Field Robotics*, vol. 33, no. 3, pp. 265–289,

[5] S. Wirth, P. L. N. Carrasco, and G. O. Codina, "Visual odometry for autonomous underwater vehicles," in *2013 MTS/IEEE OCEANS - Bergen*, Jun. 2013, pp. 1–6.

[6] T Van Damme, "Computer vision photogrammetry for underwater archaeological site recording in a low-visibility environment," *The International Archives of Photogrammetry, Remote Sensing and Spatial Information Sciences*, vol. 40, no. 5, p. 231, 2015.

[7] A. Jordt, *Underwater 3D Reconstruction Based on Physical Modelsfor Refraction and Underwater Light Propagation*, ser. Kiel Computer Science Series 2014/2. Department of Computer Science, CAU Kiel, 2014, Dissertation, Faculty of Engineering,Kiel University.

[8] R. Tsai, "A versatile camera calibration technique for high-accuracy 3d machine vision metrology using off-the-shelf tv cameras and lenses," *IEEE Journal on Robotics and Automation*, vol. 3, no. 4, pp. 323–344, Aug. 1987.

[9] A. Sedlazeck and R. Koch, "Perspective and non-perspective camera models in underwater imaging–overview and error analysis," in *Outdoor and Large-Scale Real-World Scene Analysis*, Springer, 2012, pp. 212–242.

[10] J.-M. Lavest, G. Rives, and J.-T. Lapresté, "Underwater camera calibration," in *European Conference on Computer Vision*, Springer, 2000, pp. 654–668.

[11] C. Kunz and H. Singh, "Hemispherical refraction and camera calibration in underwater vision," in *OCEANS 2008*, IEEE, 2008, pp. 1–7.

[12] E. Iscar, C. Barbalata, N. Goumas, and M. Johnson-Roberson, "Towards low cost, deep water auv optical mapping," in *OCEANS 2018 MTS/IEEE Charleston*, IEEE, 2018, pp. 1–6.

[13] Z. Zhang, "A flexible new technique for camera calibration," *IEEE Transactions on Pattern Analysis and Machine Intelligence*, vol. 22, no. 11, pp. 1330–1334, Nov. 2000.

[14] E. Iscar, K. A. Skinner, and M. Johnson-Roberson, "Multi-view 3d reconstruction in underwater environments: Evaluation and benchmark," in *OCEANS 2017 - Anchorage*, Sep. 2017, pp. 1–8.

[15] M. Bewley, A. Friedman, R. Ferrari, N. Hill, R. Hovey, N. Barrett, E. M. Marzinelli, O. Pizarro, W. Figueira, L. Meyer, R. Babcock, L. Bellchambers, M. Byrne, and S. B. Williams, "Australian sea-floor survey data, with images and expert annotations," vol. 2, 150057 EP –, Oct. 2015.

[16] M. Zhukovsky, V. Kuznetsov, and S. Olkhovsky, "Photogrammetric techniques for 3-d underwater record of the antique time ship from phanagoria," *Int. Arch. Photogramm. Remote Sens. Spat. Inf. Sci*, vol. 40, pp. 717–721, 2013.

[17] A. Sedlazeck and R. Koch, "Calibration of housing parameters for underwater stereo-camera rigs.," in *BMVC*, Citeseer, 2011, pp. 1–11.

[18] A. Jordt-Sedlazeck and R. Koch, "Refractive calibration of underwater cameras," in *Computer Vision – ECCV 2012*, A. Fitzgibbon, S. Lazebnik, P. Perona, Y. Sato, and C. Schmid, Eds., Berlin, Heidelberg: Springer Berlin Heidelberg, 2012, pp. 846–859.

[19] J. Bosch, N. Gracias, P. Ridao, and D. Ribas, "Omnidirectional underwater camera design and calibration," *Sensors*, vol. 15, no. 3, pp. 6033–6065, 2015.

[20] F. Menna, E. Nocerino, F. Fassi, and F. Remondino, "Geometric and optic characterization of a hemispherical dome port for underwater photogrammetry," *Sensors*, vol. 16, no. 1, p. 48, 2016.

[21] P. Sturm and S. Ramalingam, "A generic concept for camera calibration," in *European Conference on Computer Vision*, Springer, 2004, pp. 1–13.

[22] A. Richardson, J. Strom, and E. Olson, "AprilCal: Assisted and repeatable camera calibration," in *Proceedings of the IEEE/RSJ International Conference on Intelligent Robots and Systems (IROS)*, Nov. 2013.

[23] Sellmeier, "Zur erklrung der abnormen farbenfolge im spectrum einiger substanzen," *Annalen der Physik*, vol. 219, no. 6, pp. 272–282, 1871.

[24] B. Edlén, "The refractive index of air," *Metrologia*, vol. 2, no. 2, p. 71, 1966.

[25] R. W. Austin and G. Halikas, "The index of refraction of seawater," 1976.

[26] V. Lepetit, F.Moreno-Noguer, and P.Fua, "Epnp: An accurate o(n) solution to the pnp problem," *International Journal Computer Vision*, vol. 81, no. 2, 2009.

[27] M. Hirsch and B. Scholkopf, "Self-calibration of optical lenses," in *Proceedings of the IEEE International Conference on Computer Vision*, 2015, pp. 612–620.

[28] Y. Shih, B. Guenter, and N. Joshi, "Image enhancement using calibrated lens simulations," in *European Conference on Computer Vision*, Springer, 2012, pp. 42–56.

[29] P. Janout, J. Pospil, K. Fliegel, M. Klima, and P. Pata, "Interpolation methods for the improvement of the point spread function estimation," in *2018 28th International Conference Radioelektronika (RADIOELEKTRONIKA)*, Apr. 2018, pp. 1–5.

[30] C. J. Schuler, M. Hirsch, S. Harmeling, and B. Schlkopf, "Non-stationary correction of optical aberrations," in *2011 International Conference on Computer Vision*, Nov. 2011, pp. 659–666.

[31] D. Sage, L. Donati, F. Soulez, D. Fortun, G. Schmit, A. Seitz, R. Guiet, C. Vonesch, and M. Unser, "Deconvolutionlab2: An open-source software for deconvolution microscopy," *Methods*, vol. 115, pp. 28–41, 2017.

[32] J. L. Pech-Pacheco, G. Cristóbal, J. Chamorro-Martinez, and J. Fernández-Valdivia, "Diatom autofocusing in brightfield microscopy: A comparative study," in *Proceedings 15th International Conference on Pattern Recognition. ICPR-2000*, IEEE, vol. 3, 2000, pp. 314–317.